A Mechanically-Cooled, Highly-Portable, HPGe-Based, Coded-Aperture Gamma-Ray Imager

Klaus-Peter Ziock, Chris Boehnen, Jason Hayward, Ana C. Raffo-Caiado
Oak Ridge National Laboratory, Oak Ridge, Tennessee, USA

Abstract

Coded-aperture gamma-ray imaging is a mature technology that is capable of providing accurate and quantitative images of nuclear materials. Although it is potentially of high value to the safeguards and arms-control communities, it has yet to be fully embraced by those communities. One reason for this is the limited choice, high-cost, and low efficiency of commercial instruments; while instruments made by research organizations are frequently large and / or unsuitable for field work. In this paper we present the results of a project that mates the coded-aperture imaging approach with the latest in commercially-available, position-sensitive, High Purity Germanium (HPGe) detectors. The instrument replaces a laboratory prototype that was unsuitable for other than demonstrations. The original instrument, and the cart on which it is mounted to provide mobility and pointing capabilities, has a footprint of ~ 2/3 m x 2 m, weighs ~ 100 Kg, and requires cryogen refills every few days. In contrast, the new instrument is tripod mounted, weighs of order 25 Kg, operates with a laptop computer, and is mechanically cooled. The instrument is being used in a program that is exploring the use of combined radiation and laser scanner imaging. The former provides information on the presence, location, and type of nuclear materials while the latter provides design verification information. To align the gamma-ray images with the laser scanner data, the Ge imager is fitted and aligned to a visible-light stereo imaging unit. This unit generates a locus of 3D points that can be matched to the precise laser scanner data. With this approach, the two instruments can be used completely independently at a facility, and yet the data can be accurately overlaid based on the very structures that are being measured.

Introduction

Gamma-radiation is one of the most important observables used by the safeguards community for the control of fissile material. The value of this high-energy light comes from its ability to penetrate containers and overlying materials to reach detectors, its isotope-specific spectral properties, and its ubiquitous emission by the fissile materials of concern. As with all light, one can use it to generate images, and since fissile materials are sources, one can use such images to locate and characterize the distribution of these materials. This can be of significant benefit to the safeguards community since one of the primary indicators of malfeasance is the presence of nuclear materials where they are not supposed to be. When coupled with high-resolution spectral capabilities, such as those available from High Purity Germanium (HPGe) detectors, one can determine, not just that nuclear materials are present, but the isotopic make-up of those materials.

Unfortunately one of the primary advantages of gamma-radiation, its ability to penetrate overlying materials, also makes it difficult to image. Nevertheless, one can argue that imaging is the primary use of gamma-ray emissions by the community. Consider that even the “non-imaging” omni-directional detectors found ubiquitously throughout the safeguards community are really used to create images. These images are the final product as information is condensed to generate a map of where materials are found. The imaging information is laboriously generated by moving the instrument around a facility and recording changes in the radiation levels as a function of location. This is just low resolution imaging where the spatial resolution of the “imager” is given approximately by the distance of closest approach to a source as one sweeps past an area.

With recognition that images are important, it is not surprising that various commercial and research instruments have been developed over the years that have tried to improve on the quality of the images that are generated. What is surprising is that none of these devices have achieved wide-spread application in the community. The reluctance to embrace this technology can be attributed to the unsuitability of the instruments to the needs of the community, which can be further traced to the difficulty of generating the higher quality images. The only direct imaging approach useful at the energies of interest is a pinhole camera. This device generates images by throwing away all but a very small subset of the radiation reaching the instrument (that which enters through the pinhole).[†] A few commercial versions have been marketed, including the RadScan 800 by VT Nuclear Services [1], and the Cartogam by Canberra [2].

One can improve on the imaging efficiency of a pinhole camera by using a multiplexed or indirect imaging approach. The most efficient example is the coded aperture [3] which replaces the pinhole camera's single opening with a series of openings to let more radiation reach the detector. Each pinhole generates an image of the whole scene across the detector surface so that a mathematical unfolding must be performed to disentangle the multiple images. With care in the design of the aperture [3], the overall instrument, [4] and its application (specifically the use of a mask / anti-mask data-acquisition strategy [5]) one can generate artifact-free images that are spatially accurate with quantitative intensities. Further, if the detector has energy resolution, then the information can be accumulated in a full data cube that provides the spectra on a pixel-by-pixel basis [4].

The decrease in the time required to obtain a coded-aperture image over the equivalent image from a pinhole camera can be expressed in terms of the multiplex advantage (MA) [6, 7]. This number is the ratio of the signal-to-noise ratio (SNR) of the coded aperture image divided by that of the pinhole camera. For a single point source in the field-of-view the MA is given by the square root of the number of open pixels in the base coded-aperture pattern. In this paper we used a rank-19 mask and are planning to add a rank-31 mask, giving MAs of 13 and 22, respectively. As more and more of the field-of-view contains source material, the MA decreases since the overlapping images from the different pinholes start adding statistical noise to each other. In the limit that the whole field-of-view glows uniformly, coded apertures lose their advantage. However for most applications of interest to the safeguards community, only a small fraction of the field-of-view holds radioactive materials so that one operates in a regime where coded aperture gains are significant.

Examples of research coded-aperture imagers include [4,8-10]. Papers on their use for the control of nuclear materials include [8, 11, 12] There is at least one one commercially available product [13]. Unfortunately, it has only a modest active area (~ 16 cm^2) meaning that long acquisition times are required to generate high quality images. The instrument is based on an alkali halide scintillator detector and provides modest spectral resolution.

In this paper we report on a new compact coded-aperture imager (see Fig. 1) that combines the small size of scintillator-based cameras with the excellent energy resolution of HPGe instruments. It is constructed around a robust, commercially-available, mechanically-cooled, position-sensitive,

[†] While a parallel hole collimator may seem to increase the imaging speed by allowing all of the radiation from a given pixel to reach the surface of a detector, this is not the case since one must raster this instrument so that all of the pixels in the field-of-view are observed. One is simply trading a short dwell time on a single pixel with a lot of detector area for a longer dwell time on all pixels but with a smaller effective area. In short the efficiencies are functionally equivalent.

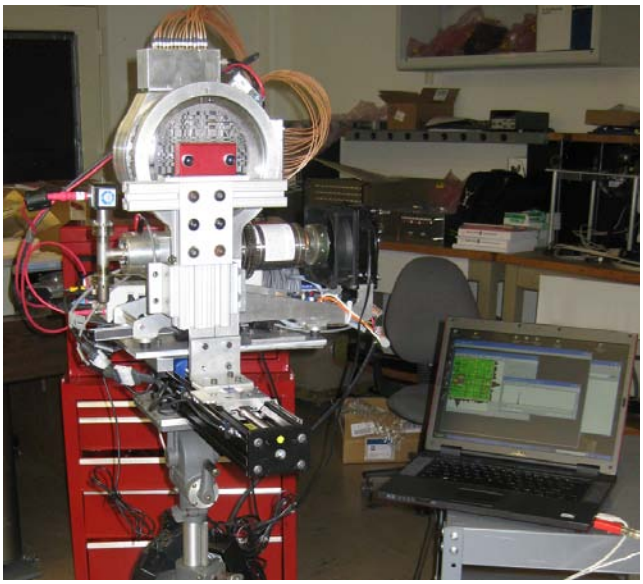

Fig. 1. The gamma-ray imager mounted on a tripod.

HPGe detector with an active area of 55 cm^2. The use of mechanical cooling provides freedom from having to refill liquid cryogens; it also enables a much smaller overall instrument because one no longer needs an attached Dewar to hold the cryogen. Further significant size reductions over a previous research prototype (see Fig. 2) [14] come from the electronics supplied with the instrument. This 32-channel system provides better performance in a package of ~ 1900 cm^3 than the 76 channels of custom electronics housed in two 19-inch rack-mount chassis' (~29,000 cm^3 each).

A further significant advance of this instrument over any approach reported previously is the inclusion of a co-aligned visible-light stereo imager. This provides visible-light images that aid in pointing the device and allows one to project the gamma-ray images on to the visible scene. Of more importance, the 3D information from the stereo pictures allows one to determine the orientation of the imager with respect to its surroundings. This aids in combining multiple gamma-ray images into a single larger image and also provides a simple mechanism to generate tomographic images of source locations in a 3D model of the environment. Examples include those available from laser scanners [15] or even from the 3D visible images themselves.

HPGe Detector

The instrument is based on a planar HPGe double-sided strip detector available from PHDs Co. [16]. The detector has an active area that is ~ 86 mm in diameter and is subdivided into strips with a 5 mm pitch. The contacts are made using an amorphous contact approach originally described by Luke and Amman. [17] The strip directions on opposite faces of the detector are orthogonal to each other with coarse event locations provided by recording the strips that collect the charge carriers. As the charges drift from the event site, they induce transitory signals on the other strip electrodes of the detector. These transitory signals are also recorded by the electronics. Their amplitudes vary based on distance from the event site and this information is used to refine the location of the event through a simple weighting process [18]. The accuracy of this refinement is dependent on knowing the depth of the event, which is obtained by recording the relative collection times of the electrons and holes [19]. At saturated velocities the drift times across the full 10 mm of the detector are ~ 100 ns. The detector is coupled to a Sunpower MT CryoTel mechanical cooler [20] by the manufacturer and the entire assembly is mounted in a cryostat that uses metal seals, to virtually eliminate the need for periodic pump-outs of the system.

Fig. 2. The prototype gamma-ray imager.

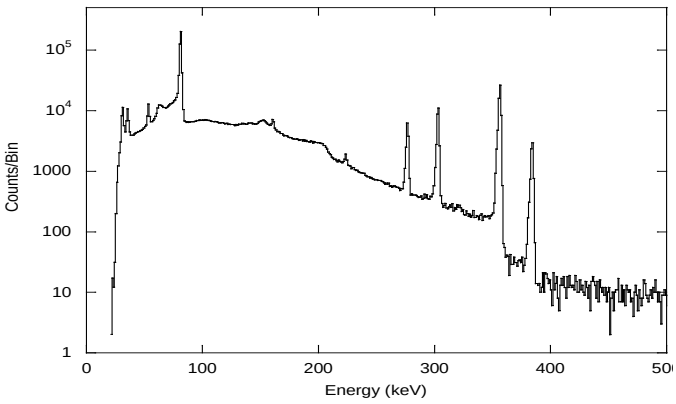

Fig. 3. ^{133}Ba spectrum from the full face of the detector.

The detector performs well, providing an electronics-limited floor to the full-face spectral resolution of 1.5 keV full width at half maximum (FWHM) (at both 81 keV and at 356 keV) with the cooler in operation (see Fig. 3).

The spatial resolution of the system is dependent on the energy of an event. This is because of the small size of the induced signals on the spectator electrodes (those on either side of a strip that actually collects charge) used to subdivide the 5 mm strips. Measured performance at the 122-keV line of ^{57}Co is ~ 1.2 mm (FWHM) in the x- and y-directions (see Fig. 4) after deconvolving the contribution of the 1 mm diameter beam width. The performance in depth is also expected to be of order a millimeter, although we do not currently use this feature other than as part of the interpolation procedure and hence have not measured it independently.

A full-face exposure of the detector reveals that there are issues associated with the interpolation approach (see Fig. 5) used to locate events to a pitch finer than that of the strips. We use an extension of the simplest approach which assigns an event to the strips that actually collect the charge and then subdivides these based on a uniform weighting of the spectator signals. The problem with the simple approach is that it does not place events into the interstrip gap. This problem has been studied at length by several authors [18, 21] but a solution suitable for use in rapid online analysis remains to be developed.

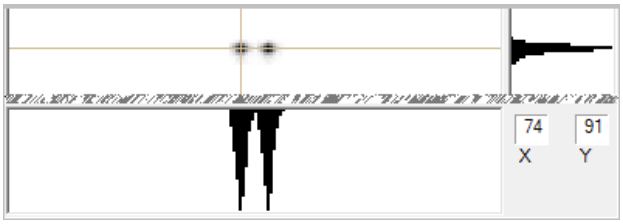

Fig. 4. An image of two exposures to a collimated beam from a ^{57}Co source separated by 4.8 mm.. The histograms to the right and below the image on the left show a histogram of the counts under the line cursors. (Note that the spots are near the vertical center of the detector but the large blank area has been cut from the image.)

We have adopted a simple approach for including events in the inter-strip gap based on the fact that up to 6.5% of charge is lost for these events, and that it is unlikely that this occurs on both sides of the detector simultaneously [22]. If two adjacent strips fire on one side and the charge loss is greater than zero but less than 6.5%, the event is placed in the gap. Although the approach does work, it does not do so uniformly. In fact the performance is better as the energy increases as can be seen in the different flood-field exposures shown in the figure. This is attributed to the fact that lower energy depositions yield smaller electron charge clouds, and, when split between adjacent strips, lower energy depositions are less likely to meet the triggering conditions on both adjacent strips. Fortunately, the performance does not significantly impact the imaging abilities if one uses a mask / anti-mask data acquisition scheme as described in the next section.

Coded Aperture Camera Design

The detector described in the preceding section is used to record the shadow pattern of the coded-aperture mask projected onto it by sources in the field of view. We have selected a modified uniformly redundant array (MURA) [23] pattern for the instrument. This class of coded apertures has

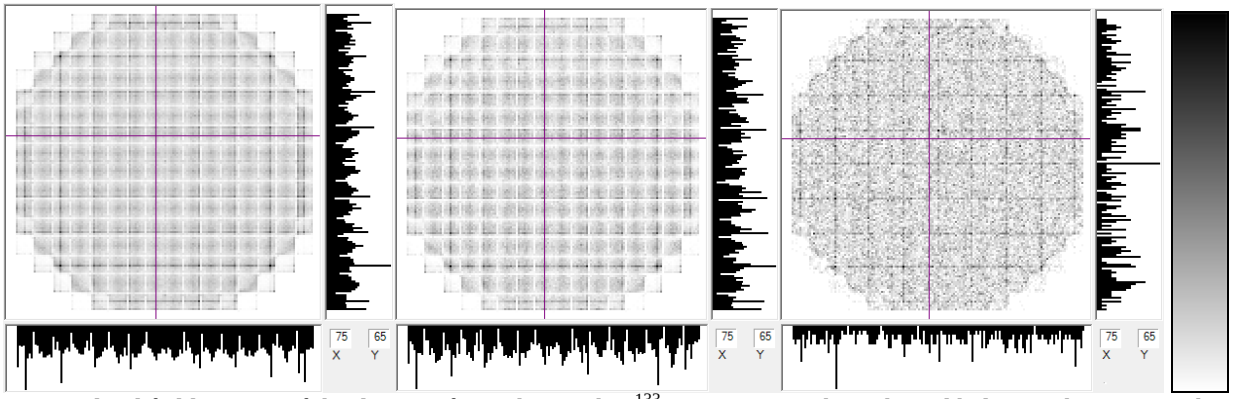

Fig. 5. Flood field images of the detector face taken with a ^{133}Ba source. To the right and below each image are histograms of the counts in the pixels under the line cursors visible in the grayscale image. The image on the left is made with the full spectrum, the center image uses just the 81-keV line and the right image uses just the 356-keV line. The structure in the images is due to incorrect interpolation of the data at the strip boundaries and is clearly worse at lower energies. The large pixels that do not have a strip on either side also show worse performance. The arbitrary grayscale intensity is given on the far right (black is more intense.)

ideal imaging properties in that it auto-correlates to a delta function, meaning that there should be no artifacts in the reconstructed images—even if there is a strong point source in the field of view. We calculate the value of the image $I_{i,j}$ in pixel (i, j) from the measured pattern at the detector, $D_{m,n}$ by performing the cross-correlation with the mask function. $M_{k,l}$: [7]

$$I_{i,j} = \sum_{k,l} M_{i+k,j+l} D_{i,j} \qquad (1)$$

The mask function is given by ±1 with the positive value used where the mask pixel is open and the negative value if the mask pixel is closed.

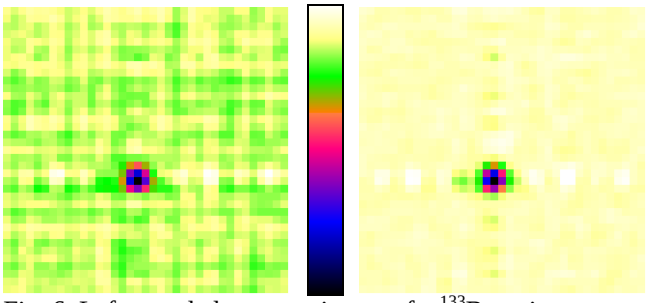

Fig. 6. Left: a coded aperture image of a ^{133}Ba point source made with only a mask exposure. The systematic structure is due to the non-uniform response of the detector at the strip boundaries. Right: the artifacts are almost completely removed by taking equal-time mask and anti-mask exposures and adding the resulting images.

Coded-aperture imaging works by encoding the image as a spatial variation in the number of counts as a function of location on the detector. An unfortunate side-effect of this is that any structure in counts versus position across the face of the detector will reconstruct as features in the image. If the variation in counts is not due to the mask pattern, then these features are undesired artifacts in the image. As noted above, there is significant high-frequency non-uniformity in the detector response function and this does cause systematic noise in the images see (Fig. 6.)

Past experience with the use of coded-aperture imagers in safeguards-type applications, has shown that there is almost always some erroneous structure in the distribution of counts as a function of position, and that this structure is frequently scene specific. Fortunately a simple and robust procedure has been developed to deal with this [7, 8]. One collects the data in two equal-time integrations, one with the mask and one with its inverse or anti-mask, (the anti-mask has the open and closed pixels reversed) and adds the two resultant images. Spatial structures not due to the mask are stationary in the two data sets. Because the sign of the mask function in equation (1) is reversed, when the images are added, the artifacts cancel while the true sources in the image add.

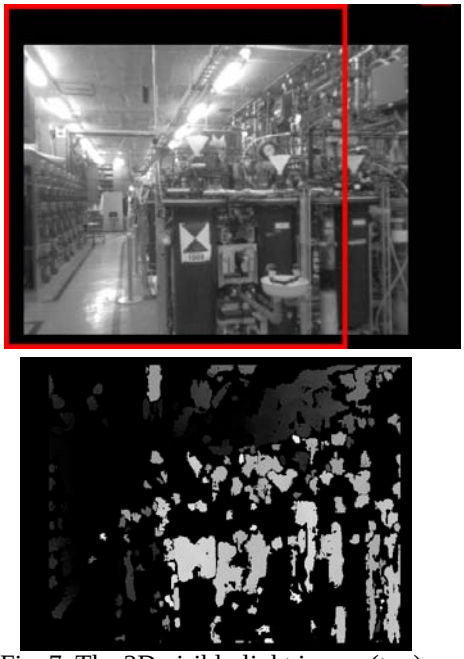

Fig. 7. The 2D visible-light image (top). The red square indicates the gamma-ray imager field of view. The 3D disparity map of the visible field (bottom).

The chief advantage of the MURA family of coded apertures is that they are their own anti-mask on a 90˚ rotation. As seen in Fig. 6 this simple approach removes almost all of the structure seen in the mask-only image.

All of the data presented in the paper was collected with a 4.5 mm thick rank-19 tungsten mask that has a pixel pitch of 2.78 mm. The mask is held in a frame that is itself mounted on three "wheels" so that the rotation between mask and anti-mask configurations can be easily achieved. A spring-loaded ball/detent assembly provides a positive indication for each of the two positions.

To minimize the apparent change in brightness as a point source location changes from the center of a single pixel to the corner between four pixels, one generally selects the mask pattern so that the detector pixels oversample it by a factor of two in each dimension [24]. In fact, for the near-field imaging case encountered in safeguards applications, one must properly oversample the detector at the mask plane where it is magnified by geometric projection effects. This means that for arbitrary source distances, one prefers to use a detector that does not have fixed pixels so that the bin sizes can be set appropriate to the source-imager geometry of a specific measurement. This is a significant advantage of the analog nature of the interpolated event position provided by this instrument.

The mask and detector are both mounted to a linear translation stage that forms the primary structural member of the instrument. The detector is fixed to the body of the stage, while the mask is mounted to the stage's slide. This allows us to change the spacing between the mask and the detector, adding a zoom capability to the instrument. There is sufficient travel to provide a *-fold zoom.

Stereo Imager

A stereo vision system is used to obtain 3D spatial information by finding the same points in the images from two calibrated 2D cameras. We utilize a commercial "STOC (Stereo on a Chip)" instrument from Videre Design [25]. It provides both a 2D and a disparity or depth map (Fig. 7). Two units with different baselines (6 cm and 30 cm) are available for providing optimum results at different target distances. Both systems are attached to a removable mount that allows them to be positioned with one camera on the optical-axis of the gamma-ray imager. The fields of view of the visible and disparity images have been calibrated to that of the gamma-ray imager. To aid operators in pointing and zooming the gamma-ray imager, the 2D visible-light image includes a square representing the instantaneous field of view of the gamma-ray camera.

Software

The instrument is controlled using software that includes a full graphical user interface (GUI). It includes the ability to point the instrument using the visible-light images from the stereo rig and then save the stereo files for archival purposes and off-line analysis. The software also controls the data collection process and displays the results as gamma-ray spectra and as false-color images of

the measured gamma-ray intensity. The results are updated in real time as the data is collected. The display is fully interactive, allowing one to view the spectra from individual, or groups of pixels in the image. The false-color image can also be changed to view the effects of selecting different spectral regions of interest (ROI). Both spectral and spatial cuts can be changed and the effects of the cuts viewed in a fully interactive fashion. Finally, the results can be saved in various formats from bitmap images through full binary list-mode data files.

The HPGe detector comes with a software suite that provides extensive control over the detector through a USB interface. This code was adapted so that it could be controlled from our own mature, coded-aperture imaging software adapted from a previous HPGe instrument [14]. Communication between the independent programs is via two memory pipes currently implemented in a Window XP environment. One of the pipes is used for command and control and allows users to run the system from within the coded-aperture imaging software. The other is used to pass data from the detector code to the coded-aperture application where it is used to generate images in real time. The imaged data is held in memory in a data-cube structure that provides a full spectrum for each pixel of the image.

The details of the various data manipulations used to form the online images are described elsewhere [4]. In short, we take advantage of the linear nature of equation (1) to generate a separate image with each of the 4096 spectral bins used by the system. This provides a data cube that can be manipulated to change the views of the data. For instance, one can obtain an image based on a different spectral ROIs by summing all of the images within the ROI into a single composite image. Alternately, one can generate the spectrum from a single (or multiple) pixels by taking the values from that pixel in each of the separate spectral images and presenting them in a histogram form.

While mathematically simple, the cross-correlation calculations used to generate the images from the detector data involve a large number of individual operations. To keep up with the online data flow, we again take advantage of the linear nature of equation (1). Before acquisition begins, and based on the zoom factor and expected distance to the source, we actually precompute the images for events that occur in each of the detector bins used in the image generation process.

Since the detector is round and the MURA mask pattern is square, the base oversampled detector (see Fig. 8) cannot take full advantage of all of the detected events. In standard coded-aperture implementations, the mask is actually made of a four-fold repetition of the base MURA pattern. A single MURA-sized section of the mask is projected onto the base oversampled detector for a source in any given pixel of the field of view. To use the extra detector area, we use a mask that is larger than this, including almost a 9-fold repetition of the base pattern. The outer elements of the mask project onto the detector area that is not included in the base square. This means some sections of the base pattern are sampled multiple times. We fold all of the data from these outer pixels back into the appropriate detector pixel of the base pattern, weighting the sum by the total detector area that samples a particular region of the mask (see Fig. 8). This technique is described in more detail in [4] and is also part of the pre-image generation.

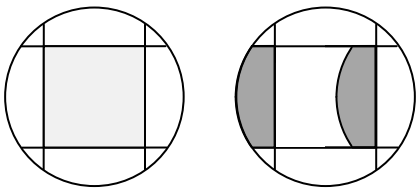

Fig. 8. (Left) The base projected mask image fills the light-grey central square of the detector. By using an oversized mask, the regions outside this square sample different parts of the same pattern. This is illustrated on the right where the two dark-gray regions sample the same part of the base mask pattern.

Performance

To date, the system has only been tested with point sources and the results clearly indicate that the performance is easily comparable to that of the much bulkier instrument on which it was based. In Fig. 9 we show images obtained with the system when a ^{133}Ba and a ^{57}Co source are in the field of view simultaneously. With only 20-s of integration time, the sources are clearly visible (top right). By placing energy ROI's on either the 356-keV or the 122-keV peak, we can also clearly identify which source is which (bottom row of the Fig.) In Fig. 10 we demonstrate the capability to provide spectra from different regions of the image. These spectra are inherently background subtracted aiding in identification of unknown sources in an image.

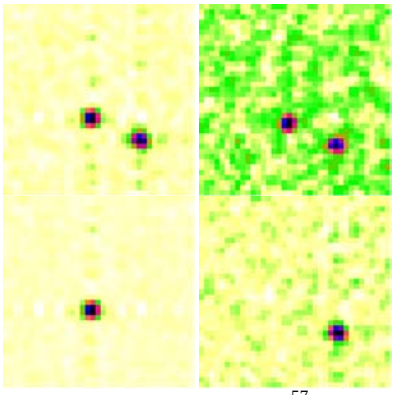

Fig. 9. Image of a 500-μCi ^{57}Co source and 1-mCi ^{133}Ba source (70 keV to 500 keV energy ROI) at a distance of ~ 225 cm from the imager (top left). The 200-s image clearly shows the presence of the sources. In fact even with only one tenth (20 s) the data the sources are still clearly visible (top right.) By setting ROI's at 122 keV (bottom left) and 356 keV (bottom right) we clearly identify the left source as the ^{57}Co and the one on the right as the ^{133}Ba.

To address concerns that non-uniformities in the detector response due to the strip-interpolation approach affect the imaging performance, we analyzed point source data collected at different energies. The results are shown in Fig. 11. In the top row are images from mask-only data cut on lines at 81 keV, 122 keV, and ~ 300 keV (from left to right respectively.) Even in this worst case, the artifacts, which are obvious at 81 keV, are significantly reduced at 122 keV. In fact, for the highest energy mask-only image, it is not clear whether the noise in the image is due to systematic or random effects. We note that the number of counts in the different peaks decreases with energy in the ratios 1:0.32:0.24. The images in the cen-

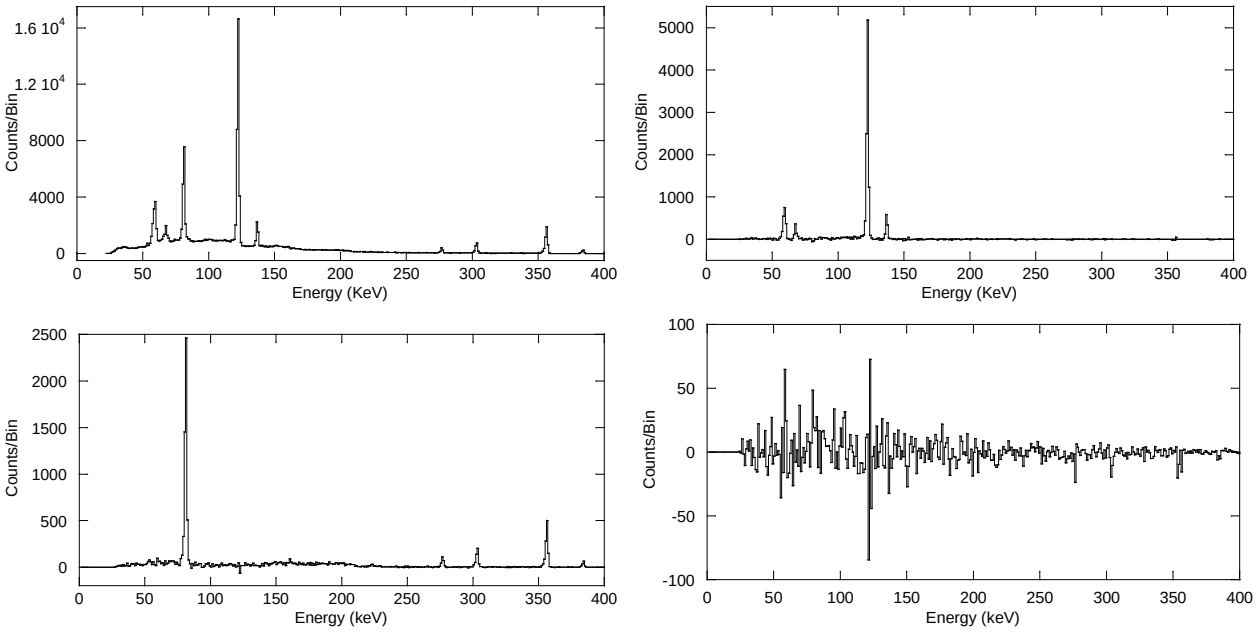

Fig. 10. Energy spectra associated with the top left image of Fig. 8. Top left is the straight spectrum from the detector. Top right is the spectrum from the peak pixel of the left source in the image. Bottom left is the spectrum from the peak pixel of the right source. In addition to providing the ability to identify the type of source, the spectra from the images are inherently background subtracted as shown by the spectrum on the bottom right which is from an arbitrary pixel in the image.

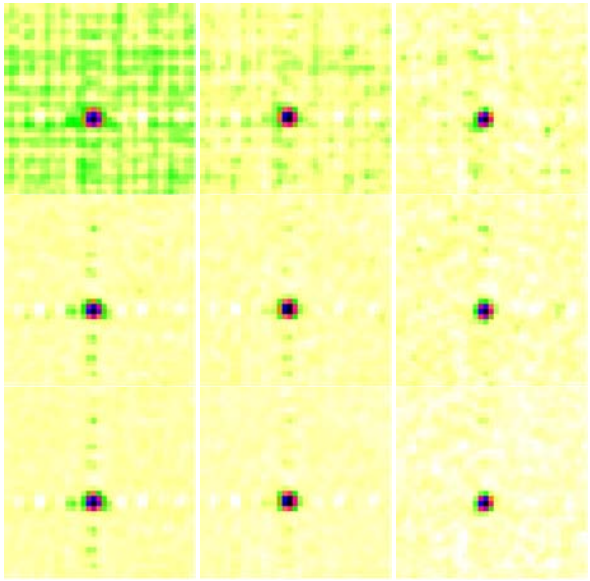

Fig. 11 The effects of systematic noise due to the strip boundaries. In the top row we show mask-only images. In the middle row are the same images using a balanced mask/anti-mask acquisition. The total acquisition times are the same. In the bottom row we show the results when twice as many counts are included in each image. From left to right, the images are made using the 81-keV peak from a ^{133}Ba source, the 122-keV line from a ^{57}Co source, and the sum of the 303-keV and 356-keV lines from the ^{133}Ba. The ratio between the counts used in each energy band is 1:0.32:0.24

ter row of Fig. 11 use the same ROI's but this time the images were made using balanced mask / anti-mask acquisitions. The total acquisition time was kept the same between the images in the two rows so that the statistical noise are the same. Finally in the bottom row we present images made using the same mask / anti-mask configurations but this time including twice as much total data.

As can be seen, the signal-to-noise ratio (SNR) improves with energy. Also, because there is little change between the images in the middle and bottom rows at 81 keV, one can infer that the systematic structures in the middle row already dominate the noise. This is not the case for the other two energies where there is some additional reduction in the noise for the higher-count images.

Since the 81-keV images have considerably more data than the images at the other two energies, one might argue that lack of improvement between the middle and bottom images is due to the fact that there are already enough counts to reach the systematic noise floor in the middle row. However we point out that even though it has only one quarter of the total counts, the bottom right image clearly has a better SNR than the one on the bottom left.

Discussion

While the highly portable nature of the imager is clearly an advantage for field work, the addition of stereo imaging potentially provides the most significant advance of the instrument. The additional information provided by the stereo images is substantial. The depth information can be utilized to facilitate alignment to a 3D laser scan as shown in Fig. 12. Although it is hard to see in still image, the information is much more useful then the simple 2D projection shown in the the other picture of the figure. The stereo date can also be used to provide lower accuracy 3D depth information to be utilized in the same manner as the laser scanner.

For instance, because one knows the distance to multiple objects in the field of view provided from the stereo images, one has the information needed to precisely determine the position of the instrument with re-

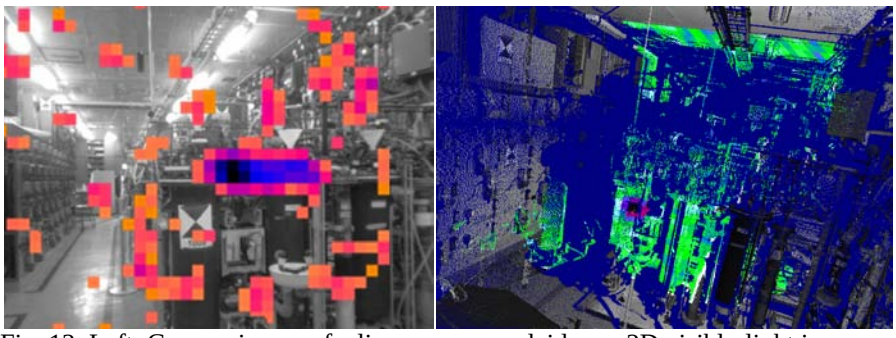

Fig. 12. Left: Gamma image of a line source overlaid on a 2D visible-light image. right: Gamma image overlaid on a 3D laser scan. (Both images were taken with the prototype gamma imager.)

spect to those objects *at the time the measurement was made*. Hence one has an accurate record of the site from which each gamma-ray image was collected and one can reliably return the instrument to this site by using objects that should be fixed. For instance in an inspection of a materials processing plant, one can rely on the processing equipment itself to verify that the instrument is at the same location for subsequent inspections. This removes concerns that fiducials marking measurement locations are altered, either accidentally or intentionally, between measurement campaigns. In addition, the 3D information can be used to help determine the distance to any sources found in the images, aiding in determination of the amount of material that may be present. Unknown distances can be best determined through simple tomographic reconstruction of multiple gamma-ray images of the same deposit collected from different locations. In this instance the 3D pictures can be used to establish the different fields of view from each location.

The instrument is clearly capable of obtaining images with a high dynamic range at energies above 100 keV. Unfortunately, below this energy the systematic artifacts associated with subdividing the 5 mm strips is clearly evident in the final images. Fortunately this does not significantly impact the value of the instrument for most safeguards applications since this is well below the emission line from one of the primary isotopes of concern—^{235}U. In fact, even with the low energy problems, there are significant advantages to having a detector that does not have a fixed pixel size. This comes from the fact that the mask pattern at the detector is magnified for objects in the near field. Since the amount of magnification is a function of the spatial resolution at the target, unless one wishes to restrict use of the instrument to specific magnifications at the source, one must accommodate a non-integral number of detector pixels per mask element at the detector. This is the approach used in our prior instrument [14] that had a fixed 2 mm pixel size. To provide freedom to take images from arbitrary distances, we always mathematically rebinned the data into bins that exactly doubled the pitch of the mask pixels at the detector. While it is effective, this procedure also introduced artifacts in the processed images, thereby limiting the overall dynamic range. However in that system, the effect occurs at all energies, not just at the lowest energies as is the case here.

Conclusion

We have developed a highly-portable gamma-ray imager based on mechanically-cooled HPGe that provides the advantages of both images and excellent spectral resolution. The instrument is coupled with a stereo-vision system that provides an additional level of information allowing easy orientation of the gamma-ray images with the real world. As the system is predominantly based on commercial components, it represents the type of instrument that could be readily adopted by the safeguards and arms-control communities and finally bring the multiple advantages of gamma-ray imaging out of the laboratory and into the real world.

References

1. VT Nuclear Services, UK B14.1 Sellafield, Seascale, Cumbria CA20 1PG, UK.
2. Canberra Industries, Inc., 800 Research Parkway, Meriden, CT 06450, U.S.A.
3. F.E. Fenimore and T.M. Cannon, *Appl. Opt.*, vol. 17, no. 3, p 337, , 1978.
4. K.P. Ziock, M.T. Burks, W. Craig, L. Fabris, E.L. Hull, N.W. Madden, *Nucl. Inst. Meth in Phys. Res. B*, vol. 505, p. 420, 2003.
5. C. Brown, *J. Appl. Phys.*, vol. 45, no. 4, p. 1806, 1974.
6. C.M. Brown, Ph.D. thesis, "Multiplex Imaging and Random Arrays," U. Chicago (1972).
7. E.E. Fenimore, *Appl. Opt.*, vol. 17, p. 3562, Nov. 1978.

8. K.P. Ziock, T.B. Gosnell, C.J. Hailey, J.H. Lupton, F.A. Harrison, *IEEE Trans. Nucl. Sci.*, vol. 39, p. 1046, 1992.
9. K.P. Ziock, L. Nakae,. *IEEE Trans. Nucl. Sci.*, vol. 49, p. 1552, 2002.
10. M. Woodring, et al., *Nucl. Inst. Meth in Phys. Res. A*, vol. 422, p. 709, 1999.
11. K.P. Ziock, L. Madison, B.R. McGinnis, R.R. Royce and Angela Brown, "Proc. of the 36th Annual INMM meeting," Palm Desert Ca., July 9-12, 1995.
12. K.P. Ziock, L. Madison, "Proc. of the 36th Annual INMM meeting," Palm Desert Ca., July 9-12, 1995.
13. RADCAM from Radiation Monitoring Devices, Inc., 44 Hunt Street, Watertown, MA 02472.
14. K.P. Ziock, M.T. Burks, C.P. Cork, E.L. Hull, N.W. Madden, "Proc. IEEE Nucl. Sci. Symp.," Portland, Oregon, Oct. 2003.
15. L. Mihailescu, et al., in Proc. INMM Annual Meeting, Nashville, TN 2006.
16. PHDs Co., 777 Emory Valley Rd, Suite B, Oak Ridge, TN 37830.
17. P.N. Luke et al., *IEEE Trans. Nuc. Sci.*, vol. 39, p. 590, 1992.
18. M. Amman, P.N. Luke, *Nucl. Inst. Meth in Phys. Res. A*, vol. 452, p. 155, 2000.
19. M. Burks et al., in *IEEE NSS Conf. Record*, vol. 2, p. 1114, 2004.
20. Sunpower, Inc., 182 Mill Street, Sunpower, Inc., Athens, Ohio 45701.
21. G. Rossi, J. Morse, D. Protic, *IEEE Trans. Nuc. Sci.*, vol. 46, p. 765, 1999.
22. J.P. Hayward, D.K. Wehe, *IEEE Trans. Nuc. Sci.*, vol. 55, p. 2789, 2008.
23. S. Gottesman and E. Fenimore, *Appl. Opt.*, vol. 28, p. 4344, 1989.
24. E. Caroli, et al., *Space Sci. Rev.*, vol. 45, p. 349, 1987.
25. Videre Design LLC, 865 College Ave., Menlo Park, CA 94025.